Alkali-metal-atom polarization imaging in high-pressure optical-pumping cells

A. Ben-Amar Baranga, S. Appelt, C. J. Erickson, A. R. Young, and W. Happer
Joseph Henry Laboratory, Physics Department, Princeton University, Princeton, New Jersey 08544
(Received 14 November 1997)

We present a detailed experimental analysis of Rb-polarization imaging in high-pressure gas cells. The Rb vapor in these cells is optically pumped by high-power diode-laser arrays. We present images for high (35 G) and low (4 G) magnetic fields and for different He and Xe buffer-gas mixtures. We demonstrate that high-field imaging provides an absolute measurement of the Rb-polarization distribution in the cell, based on the fact that a spin-temperature distribution of the hyperfine magnetic sublevels is established in high-pressure buffer gases. A survey of various mechanisms that broaden the Rb magnetic-resonance lines is presented. These broadening mechanisms determine the limits of the spatial resolution achievable for images of the Rb-polarization distribution. [S1050-2947(98)04109-2]

PACS number(s): 32.80.Bx, 32.80.Cy, 32.70.Jz

I. INTRODUCTION

The production of hyperpolarized noble gases through spin exchange with optically pumped alkali-metal atoms has been important for a large variety of fields, among them magnetic resonance imaging [1–6], materials and surface sciences [7–10], atomic physics [11–13], and in nuclear physics measurements such as the determination of the spin structure of the neutron [14]. The present work is motivated by a desire to increase the quantity and the polarization of the hyperpolarized noble gas produced. The total noble-gas nuclear polarization produced by spin-exchange optical pumping depends on the three-dimensional distribution of the Rb spin polarization. A reliable method of measuring the spatial distribution of the alkali-metal polarization should provide helpful information in the development of effective optical-pumping techniques. An imaging technique in very low magnetic field using laser optical pumping in a rotating magnetic field gradient has recently been published [15]. In this paper we present an imaging technique for high-pressure optical-pumping cells, in high and low magnetic fields [16]. We focus on Rb vapor pumped by broadband high-power diode-laser arrays [2–4 nm full width at half maximum (FWHM)]. The high-pressure buffer gas broadens the Rb optical transition linewidth, leading to a more efficient optical coupling to the diode-laser array emission. At the buffer-gas pressures explored in this work ($\approx$10 atm), the spatial diffusion of the Rb atoms is negligible [17]. The Rb polarization is effectively ''frozen'' into the vapor. An additional, interesting finding is that optical pumping under high-pressure conditions generally leads to a spin-temperature distribution of Rb atoms between the hyperfine magnetic sublevels.

This paper is organized as follows. Section II reviews the salient theoretical considerations leading to a complete characterization of an alkali-metal-atom polarization in high-pressure cells. This section also presents the basic theory of gradient polarization imaging, including considerations of achievable spatial resolutions. In Sec. III the experimental apparatus and procedure for measuring Rb polarization images is described. The experimental results are presented in Sec. IV along with numerical simulations. In particular, we present data confirming the existence of a spin-temperature distribution, absolute Rb polarization measurements as a function of optical-pumping rate, and Rb-linewidth measurements. We present various Rb-polarization images including hole burning effects under very high optical-pumping rates, in high and low magnetic fields. We conclude in Sec. V with a brief survey of the possible implications of this work for future investigations and applications.

II. THEORY

We consider here Rb vapors, optically pumped by an intense laser beam propagating along the z (longitudinal) axis of a coordinate system. A weak probe beam, a few millimeters in diameter, propagates through the vapor at right angles to the pumping beam in the direction

$$\mathbf{n}=\mathbf{x}\cos\alpha+\mathbf{y}\sin\alpha. \tag{1}$$

The probe beam is circularly polarized so the mean photon spin is $\mathbf{s}=s_n\mathbf{n}$ for probe light of helicity $s_n=\mathbf{s}\cdot\mathbf{n}=\pm1$.

The atoms are subject to a longitudinal magnetic field B_z. Along the path of the probe beam, B_z has a uniform part B_z' and an approximately linear spatial gradient. A small transverse magnetic field, oscillating at a frequency ω close to the Zeeman resonance frequencies of the alkali-metal atom, defines the x axis of the coordinate sytem, so the total magnetic field is

$$\mathbf{B}=2B_1\mathbf{x}\cos\omega t+(B_z'+l\partial B_z/\partial l)\mathbf{z}. \tag{2}$$

Here the distance along the path of the probe beam from the midpoint of the cell is l. We have omitted from Eq. (2) small additional terms needed to ensure that $\nabla\cdot\mathbf{B}=0$. These terms would have no influence on the subsequent perturbation-theory calculations.

The probe laser is tuned close to the D_1 resonance line of the alkali-metal vapor. The attenuation of the probe-beam intensity I is given by

$$\frac{\partial I}{\partial l}=-\kappa(1-2s_n\langle S_n\rangle)I. \tag{3}$$

The attenuation coefficient is $\kappa=[\mathrm{Rb}]\sigma$ where [Rb], assumed uniform in the cell, is the number density of Rb atoms and σ is the photon absorption cross section per unpolarized atom. $\langle S_n\rangle$ is the transverse electron spin polarization that oscillates at the rf drive frequency ω. For light of pure circular polarization, the mean spin ($s_n=\pm 1$) does not change as the light passes through the polarized Rb vapor. The helicity of any other state of photon polarization could grow or diminish monotonically as the light propagates through the vapor.

Integrating Eq. (3) over the total path length L through the vapor, we find that the intensity I_L of the probe beam as it emerges from the vapor is

$$I_L=e^{-\kappa L}I_0\exp\left\{2\kappa s_n\int_{-L/2}^{L/2}\langle S_n\rangle dl\right\}. \tag{4}$$

The vapor is often very optically thick for photons close to the center of the D_1 absorption line, so the probe laser is detuned to ensure that $\kappa L<1$. The radio-frequency field that generates $\langle S_n\rangle$ is always kept sufficiently small that $|2\kappa L\langle S_n\rangle|\ll 1$. Then the second exponential function of Eq. (4) is well approximated with the first two terms of a power series and we find

$$I_L=e^{-\kappa L}I_0+e^{-\kappa L}I_0 2\kappa s_n\int_{-L/2}^{L/2}\langle S_n\rangle dl. \tag{5}$$

The transmitted probe intensity I_L is measured with a photodetector and the component at the rf drive frequency ω is detected with a lock-in amplifier, with an integration time constant $\tau\gg\omega^{-1}$ and with a phase shift θ between the peak of the reference signal and the peak of the the rf magnetic field $B_1\cos\omega t$. The output voltage of the lock-in amplifier is

$$V=G\int_{-L/2}^{L/2}\overline{\langle S_n\rangle}dl \quad \text{with} \quad G=I_0e^{-\kappa L}2\kappa s_n\xi. \tag{6}$$

The coefficient G includes a factor ξ to account for the gain of the lock-in amplifier, the efficiency of the photodetector, various reflection losses of the probe beam at glass surfaces, etc. The signal, as processed by the lock-in amplifier, is

$$\overline{\langle S_n\rangle}=\frac{2}{\tau}\int_0^\infty dt'\langle S_n(t-t')\rangle e^{-t'/\tau}\cos\{\omega(t-t')-\theta\}, \tag{7}$$

where $\overline{\langle S_n\rangle}$ is a function of position l along the probe beam and normally varies slowly with time t as the uniform field B_z' sweeps through the resonance region.

Let the alkali-metal atom have nuclear spin I and two Zeeman multiplets (for $I>0$) with total angular momentum (in the low-field limit) $f=a=I+1/2$ and $f=b=I-1/2$. The Zeeman resonance frequencies for transitions between the sublevels $|fm\rangle$ and $|f,m-1\rangle$ with energies $E(fm)$ and $E(f,m-1)$ and mean azimuthal quantum number $\overline{m}=m-1/2$ are

$$\omega_{f\overline{m}}=(E_{fm}-E_{f,m-1})/\hbar. \tag{8}$$

Physically meaningful values of $\overline{m}$ occur in the range $-I\leqslant\overline{m}\leqslant I$. We will often interpret $\overline{m}$ as an azimuthal quantum number of the nuclear spin operator I_z. The resonance frequencies $\omega_{f\overline{m}}$, correct to second order in the magnetic field, are [18]

$$\omega_{a\overline{m}}=\frac{B_z(g_S\mu_B-2\mu_I)}{\hbar[I]}-\frac{B_z^2\overline{m}\,2(g_S\mu_B+\mu_I/I)^2}{[I]^2\hbar^2\omega_{\mathrm{hf}}}, \tag{9}$$

$$\omega_{b\overline{m}}=-\frac{B_z(g_S\mu_B+\{2+2/I\}\mu_I)}{\hbar[I]}+\frac{B_z^2\overline{m}\,2(g_S\mu_B+\mu_I/I)^2}{[I]^2\hbar^2\omega_{\mathrm{hf}}}. \tag{10}$$

The g value of the electron is $g_S=2.002\,32$, $\mu_B=9.2741\times10^{-21}$ erg G^{-1} is the Bohr magneton, μ_I is the nuclear magnetic moment, and $\hbar\omega_{\mathrm{hf}}=[I]A/2$ is the energy splitting of the Zeeman multiplets a and b at zero magnetic field. Here and subsequently, a spin quantum number in square brackets denotes the statistical weight of the spin sublevels, for example, $[I]=2I+1$. To first order in B_z, the resonance frequencies $\omega_{a\overline{m}}$ and $\omega_{b\overline{m}}$ are of opposite signs and are independent of $\overline{m}$. They differ in magnitude by a few parts per thousand because of the contribution of the nuclear moment μ_I to the precession frequencies. To second order in B_z, the resonance frequencies have a ''quadratic splitting,'' proportional to $B_z^2\overline{m}$. The quadratic splitting is the same for both Zeeman multiplets.

In practice, it is straightforward to choose magnetic fields B_z large enough to ensure that the quadratic splittings of Eqs. (9) and (10) exceed the resonance damping rates $\gamma_{f\overline{m}}$, due to various relaxation processes, which we will discuss below. For this condition of good intrinsic resolution,

$$|\omega_{f\overline{m}}-\omega_{f\overline{m}\pm1}|\approx\frac{2(g_S\mu_B)^2B_z^2}{[I]^2\hbar^2|\omega_{\mathrm{hf}}|}\gg\gamma_{f\overline{m}}, \tag{11}$$

where each resonance will contribute independently to $\overline{\langle S_n\rangle}$ of Eq. (6) to give [19]

$$\begin{aligned}\overline{\langle S_n\rangle}=&\frac{g_S\mu_BB_1s_n}{8[I]^2\hbar}\sum_{\overline{m}}([a]^2-4\overline{m}^2)\\&\times PQ_{\overline{m}}\frac{(\omega_{a\overline{m}}-\omega)\cos(\theta-\alpha)+\gamma_{a\overline{m}}\sin(\theta-\alpha)}{(\omega_{a\overline{m}}-\omega)^2+\gamma_{a\overline{m}}^2}\\&+\frac{g_S\mu_BB_1s_n}{8[I]^2\hbar}\sum_{\overline{m}}([b]^2-4\overline{m}^2)\\&\times PQ_{\overline{m}}\frac{(\omega_{b\overline{m}}+\omega)\cos(\theta+\alpha)-\gamma_{b\overline{m}}\sin(\theta+\alpha)}{(\omega_{b\overline{m}}+\omega)^2+\gamma_{b\overline{m}}^2}.\end{aligned} \tag{12}$$

The signal (12) is a function of position l along the probe beam and time t. It varies slowly with time t as the uniform field B_z' and consequently the resonance frequencies $\omega_{f\overline{m}}$ are swept through the resonance region. Unless the field gradient $\partial B_z/\partial l$ of Eq. (2) is zero, the resonance frequencies $\omega_{f\overline{m}}$ are functions of position l. The amplitudes of the resonances $f\overline{m}$ are proportional to the product $PQ_{\overline{m}}$ of the overall polariza-

tion P and the probability $Q_{\bar{m}}$ that the nuclear spin will have the azimuthal quantum number $\bar{m}$. Both P and $Q_{\bar{m}}$ will normally depend on l.

Equation (12) is valid when the density matrix of the alkali-metal atoms is well approximated by the spin-temperature distribution

$$\rho=\frac{e^{\beta F_z}}{Z}=\frac{e^{\beta I_z}e^{\beta S_z}}{Z_I Z_S}, \tag{13}$$

introduced by Anderson *et al.* [20] The spin-temperature distribution (13) will prevail for the high-pressure conditions of spin-exchange optical pumping, whether or not the spin-exchange rate between alkali-metal atoms is the fastest relaxation rate of the system.

The *Zustandssumme* $Z=Z_I Z_S$ is the product of a nuclear part Z_I and an electronic part Z_S, where for a spin of integer or half-integer quantum number J,

$$Z_J=\sum_{m=-J}^{J} e^{\beta m}=\frac{\sinh \beta[J]/2}{\sinh \beta/2}=\frac{(1+P)^{[J]}-(1-P)^{[J]}}{2P(1-P^2)^J}. \tag{14}$$

The spin-temperature distribution can be characterized with an overall polarization P, defined in terms of the mean electron spin $\langle S_z\rangle$ and the spin-temperature parameter β by

$$P=2\langle S_z\rangle=\tanh\frac{\beta}{2} \quad \text{or, conversely,} \quad \beta=\ln\frac{1+P}{1-P}. \tag{15}$$

The factors

$$Q_{\bar{m}}=\frac{e^{\beta\bar{m}}}{Z_I}=\frac{2P(1+P)^{I+\bar{m}}(1-P)^{I-\bar{m}}}{(1+P)^{[I]}-(1-P)^{[I]}} \tag{16}$$

of Eq. (12) are the probabilities that the nuclear spin has the azimuthal quantum number $\bar{m}$. One can readily show that $Q_{\bar{m}}\to 1/[I]$ as $P\to 0$ and $Q_{\bar{m}}\to\delta_{\bar{m},I}$ as $P\to 1$.

The damping rates $\gamma_{f\bar{m}}$ of Eq. (12) are [19]

$$\begin{aligned}\gamma_{f\bar{m}}=&\left(\frac{1}{T_{\rm ex}}+\frac{1}{T_{\rm SD}}+R\right)\left(\frac{3[I]^2+1-4\bar{m}^2}{4[I]^2}\right)\\&-\left(\frac{P}{T_{\rm ex}}+Rs_z\right)\frac{\bar{m}}{[I]}(-1)^{a-f}\\&+\left(\frac{1}{T_{\rm FD}}-\frac{\eta Q_{\bar{m}}}{T_{\rm ex}}\right)\frac{[f]^2-4\bar{m}^2}{4[I]^2}.\end{aligned} \tag{17}$$

Here R is the local optical-pumping rate, which can be written as $R=\alpha I_l$, where I_l is the power of the pumping laser and α is a coefficient depending on the spectral profile of the pumping light and the alkali-metal atom absorption line [19]. $s_z=\pm 1$ is the mean photon spin for the circularly polarized pumping light. The S-damping rate $1/T_{\rm SD}$ comes from interactions with correlation times much shorter than the hyperfine period and therefore is capable of causing both $\Delta f=0$ and $\Delta f=\pm 1$ transitions. The term proportional to $1/T_{\rm FD}$ is due to interactions with correlation times much longer than the hyperfine period and therefore is only capable of causing $\Delta f=0$ transitons between sublevels in the same Zeeman multiplet. This form of relaxation occurs only when the alkali-metal atoms form long-lived van der Waals molecules. In the high gas pressures characteristic of spin-exchange optical pumping, most of the van der Waals molecules break up so quickly that they contribute only to S damping, so we can usually ignore $1/T_{\rm FD}$ compared to $1/T_{\rm SD}$. The spin-exchange rate of the resonating alkali-metal atom with all other alkali-metal atoms is $1/T_{\rm ex}$. The fraction of like isotopes is η; for example, if Eq. (17) describes the widths of ^{85}Rb magnetic resonances for a natural isotopic mixture, $\eta=0.7215$.

For the conditions explored in this work, the Rb spin destruction rate is dominated by collisions with buffer-gas atoms (He and Xe). Interpretation of the damping rates is more complicated when Rb-Rb collisions make a significant contribution to the spin destruction rate. Experiments by Walker *et al.* [21] have shown that Rb-Rb spin destruction rates can be slowed by tens of percent by magnetic fields of a few thousand gauss. A detailed, consistent description of the physics of Rb-Rb collisions that incorporates these findings is not yet available.

Under the high-pressure conditions of spin-exchange optical pumping where $1/T_{\rm FD}$ can be neglected, the local polarization produced in the vapor is independent of the spin-exchange rate and given simply by [19]

$$P=s_z\frac{RT_{\rm SD}}{1+RT_{\rm SD}}. \tag{18}$$

For a sufficiently large field gradient in Eq. (2) the rf field produces one or more resonant surfaces in the vapor where the signal (12) is maximum (because the resonant denominators are minimum). The signal diminishes at increasing distances from the resonant surface. The contribution to $\overline{\langle S_n\rangle}$ from the precessing atoms can therefore occur along a relatively small increment Δl of the probe beam, where it crosses the resonant surface, and this makes gradient imaging possible.

One can choose the lock-in phase angle θ and the direction α of the probe beam to eliminate the dispersive parts of Eq. (12), proportional to $\omega_{a\bar{m}}-\omega$ and $\omega_{b\bar{m}}+\omega$, leaving purely Lorentzian curves. For $I>0$ there are two fundamentally different possibilities, which we denote with an index $j=x$ or y. In one case, which we denote with $j=x$, the probe beam is parallel to the x axis, the direction of oscillation of the rf field, $\alpha=0$, and $\theta=\pi/2$. In the other case, which we denote with $j=y$, the probe beam is parallel to the y axis and perpendicular to the direction of oscillation of the rf field, $\alpha=\pi/2$, and $\theta=0$. In either case the coefficients of all dispersive terms in Eq. (12) vanish, that is, $\cos(\theta-\alpha)=0$ and $\cos(\theta+\alpha)=0$. The coefficients of the Lorentzian terms are proportional to

$$u_{fj}=-\sin(\alpha-\theta[-1]^{a-f})=\begin{cases}1 & \text{if} \quad f=a, \quad j=x\\ -1 & \text{otherwise.}\end{cases} \tag{19}$$

Adding π to either α or θ simply changes the sign of all terms in Eq. (19). So the Lorentzians of Eq. (12) have oppo-

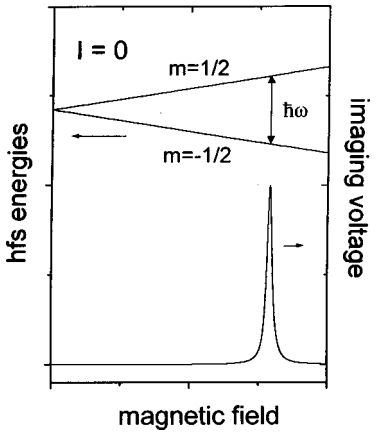

FIG. 1. Zeeman energy levels of the ground state of a hypothetical alkali-metal atom with $I=0$. The lower trace describes the Zeeman spectrum in a uniform magnetic field B_z', described by the voltage in Eq. (6). Experimentally, this spectrum is obtained by sweeping the uniform field or the applied rf frequency ω.

site signs in the Zeeman multiplets $f=a$ and b for a probe beam along the x axis and they have the same sign for a probe beam along the y axis.

A. Example for $I=0$

To illustrate how the imaging works, we will first consider a hypothetical alkali-metal atom with $I=0$ and with the two Zeeman energy levels sketched in Fig. 1. Most of the insights gained from examining this simple example carry over to the case of real atoms with $I>0$.

If $I=0$, there is only one Zeeman multiplet (doublet) and one resonance with $f=a=1/2$, $\bar{m}=0$. Then the sum (12) consists of a single resonance with $Q_{\bar{m}}=Q_0=1$. The dispersive term of Eq. (12) can be eliminated for any probe direction by setting $\theta=\alpha+\pi/2$, giving

$$\overline{\langle S_n\rangle}=\frac{g_S\mu_B B_1 s_n}{2\hbar}\,\frac{P\gamma_0}{(\omega_0-\omega)^2+\gamma_0^2}, \tag{20}$$

where for simplicity we have set $\omega_{a\bar{m}}=\omega_0$ and $\gamma_{a\bar{m}}=\gamma_0$. The resonance frequency is

$$\omega_0=\omega_0'+l(\partial\omega_0/\partial l), \tag{21}$$

where we find from Eq. (9) $\omega_0'=B_z' g_S\mu_B/\hbar$ and $\partial\omega_0/\partial l=(\partial B_z/\partial l)g_S\mu_B/\hbar$.

We define an image coordinate l' by

$$l'=(\omega-\omega_0')(\partial\omega_0/\partial l)^{-1}. \tag{22}$$

Here the prime is used to denote both a spatially uniform quantity ω_0' and the related image coordinate l', which is independent of the object coordinate l. By changing the uniform field B_z' and the corresponding Zeeman frequency ω_0', we can scan the image coordinate l' over an interval that includes the interval $[-L/2,L/2]$ of the object coordinate l. Then the voltage (6) becomes

$$V(l')=MJ(l'), \tag{23}$$

where the coefficient is

$$M=\pi G B_1 s_n(2\partial B_z/\partial l)^{-1}. \tag{24}$$

The image is

$$J(l')=\int_{-L/2}^{L/2}H(l',l)P(l)dl \tag{25}$$

and the point-spread function is

$$H(l',l)=\frac{b/\pi}{(l'-l)^2+b^2}. \tag{26}$$

The linewidth of the point-spread function is

$$b=b(l)=\gamma_0(\partial\omega_0/\partial l)^{-1} \quad \text{with} \quad \gamma_0=R+\frac{1}{T_{\mathrm{SD}}}. \tag{27}$$

The optical-pumping rate is R and the S-damping rate is $1/T_{\mathrm{sd}}$. R will ordinarily depend on l, both because of inhomogeneities of the laser source and because of attenuation of the pumping light in the vapor. The point-spread function $H(l',l)$ of Eq. (26), also called the impulse-response function, or the Green's function in related problems, has the same significance in gradient imaging as does the Airy disk of a conventional lens system for optical imaging. It has unit area in image space

$$\int_{-\infty}^{\infty}H(l',l)dl'=1. \tag{28}$$

In many cases of practical interest, the point-spread function (26) will also have very nearly unit area in object space, but this is not a rigorous area theorem like Eq. (28), because the width $b=b(l)$ depends on position l in object space.

Equation (28), together with Eq. (25), implies that the image and object have the same areas

$$\int_{-\infty}^{\infty}J\,dl'=\int_{-L/2}^{L/2}P\,dl. \tag{29}$$

In special cases, for example, a uniform S-damping rate $1/T_{\mathrm{SD}}$ throughout the cell and a very weak optical-pumping rate R, the width (27) and the point-spread function are independent of location l of the object point. Then the point-spread function (26) will depend only on $l'-l$, a property often called shift invariant or isoplanatic. There is a large body of literature on how spatial Fourier transforms can be used to analyze the imaging quality of isoplanatic systems [22]. However, for studies of spin-exchange optical pumping, where high optical-pumping rates and high polarizations are of interest, the imaging is basically anisoplanatic because the point-spread function is significantly broader where the light intensity is higher. As long as the width b remains small compared to the length scale for substantial spatial variations of P, this anisoplanatism will have negligible effect on the image quality. Then the point-spread function (26) will have approximately a unit area in object space and will behave much like a Dirac δ function and the image (25) will become

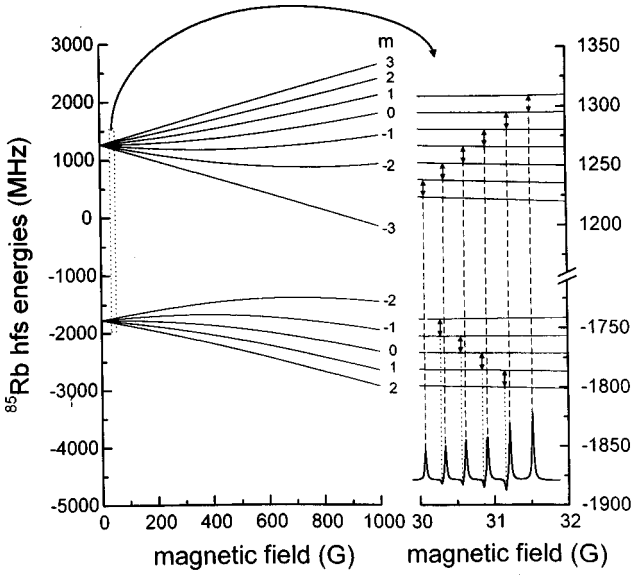

FIG. 2. ^{85}Rb Zeeman energy levels. The right corner lower trace describes the Zeeman spectrum in a uniform magnetic field B_z', described by the voltage in Eq. (6), measured by sweeping the uniform field or the applied rf frequency ω.

$$J(l') \approx P(l'). \tag{30}$$

If b varies strongly enough along the probe beam, for example, because of large variations of R, the image will have substantial aberrations. In this case, Eq. (30) can serve as the first approximation of an iterative determination of the true object function $P(l)$ from the experimentally determined image function $J(l')$.

We conclude the discussion of this simple example by noting that the experimentally measured voltage (23) is only proportional to $J(l')$ so the coefficient of proportionality M is needed to get an absolute polarization. M is difficult to determine experimentally because of the need to accurately measure the number density [Rb], the attenuation coefficient κ, the reflection losses, rf field amplitudes, the efficiency of the photodetector, the gain of the lock-in amplifier, etc. So for the hypothetical atom with $I=0$ it would be comparatively easy to measure a relative polarization $P(l') \propto V(l')$, but more difficult to measure an absolute polarization. This problem can be largely overcome with real alkali-metal atoms, with nuclear spin quantum numbers $I>0$, to which we now turn our attention. We will illustrate our discussion with ^{85}Rb, for which the nuclear spin is $I=5/2$ and for which the energy levels are sketched in Fig. 2.

B. Imaging with well-resolved, quadratically split resonances

Consider first the case of resonances with good intrinsic resolution, satisfying the criterion (11), and for which $\overline{\langle S_n \rangle}$ is given by Eq. (12). The field gradient $\partial B_z/\partial l$ is small enough that no more than one resonance can be excited in the cell, that is,

$$\left|\frac{\partial B_z}{\partial l}\right| < \frac{2 g_S \mu_B B_z^2}{[I] L \hbar |\omega_{\rm hf}|}. \tag{31}$$

In analogy to Eq. (22), an image-space coordinate can be defined for each Zeeman resonance $f\bar{m}$,

$$l' = ([-1]^{a-f}\omega - \omega'_{f\bar{m}})(\partial \omega_{f\bar{m}}/\partial l)^{-1}, \tag{32}$$

with $\omega'_{f\bar{m}}$ determined by the uniform field B_z' through Eqs. (9) and (10). Each resonance defines a point-spread function

$$H_{f\bar{m}}(l',l) = \frac{b_{f\bar{m}}/\pi}{(l'-l)^2 + b_{f\bar{m}}^2}, \tag{33}$$

where the width is

$$b_{f\bar{m}} = \gamma_{f\bar{m}} |\partial \omega_{f\bar{m}}/\partial l|^{-1}. \tag{34}$$

When the uniform field B_z' is scanned, the voltage (6) will consist of a series of peaks

$$V_{f\bar{m},j}(l') = M_{f\bar{m}} u_{fj} \frac{[f]^2 - 4\bar{m}^2}{4[I]^2} J_{f\bar{m}}(l'), \tag{35}$$

each of which can be associated with one of the resonances $f\bar{m}$, and the index $j=x$ or y which specifies the axis along which the probe beam propagates. In analogy to Eq. (24), the coefficient is

$$M_{f\bar{m}} = \pi G g_S \mu_B B_1 s_n |2\hbar \partial \omega_{f\bar{m}}/\partial l|^{-1} \approx [I] M. \tag{36}$$

For the relatively small magnetic fields needed for good resolution, one can verify from Eqs. (9) and (10) that the gradients $\partial \omega_{f\bar{m}}/\partial l$ differ by less than 1% for adjacent resonances $f\bar{m}$ and $f,\bar{m}\pm 1$. Thus, the coefficients $M_{f\bar{m}}$ and $M_{f,\bar{m}\pm 1}$ are nearly the same and as indicated in Eq. (36) are very nearly a factor of $[I]$ larger than the coeffient M of Eq. (24) for the hypothetical atom with $I=0$.

The image is

$$J_{f\bar{m}}(l') = \int_{-L/2}^{L/2} H_{f\bar{m}}(l',l) P(l) Q_{\bar{m}}(l) dl. \tag{37}$$

In analogy to Eq. (28), the point-spread function (33) has unit area in image space and an area theorem, analogous to Eq. (29), holds,

$$\int_{-\infty}^{\infty} J_{f\bar{m}} dl' = \int_{-L/2}^{L/2} P Q_{\bar{m}} dl. \tag{38}$$

Finally, in analogy to Eq. (30), if the product $P(l)Q_{\bar{m}}(l)$ does not change too rapidly in object space compared to the width (34), the point-spread function (33) behaves much like a Dirac δ function in object space and we can write Eq. (37) as

$$J_{f\bar{m}}(l') \approx P(l') Q_{\bar{m}}(l'). \tag{39}$$

We see from Eqs. (35) and (39) that the lock-in voltages $V_{f\bar{m},j}(l')$ are very nearly proportional to the product of the electron polarization $P(l')$ and the probability $Q_{\bar{m}}(l')$ that the nucleus has the azimuthal quantum number $\bar{m}$. One can largely eliminate the calibration problem for well-resolved image voltages by taking ratios of image voltages $V_{f\bar{m},j}$ for adjacent resonances. This cancellation of poorly known calibration factors remains valid when the field gradients $\partial \omega_{f\bar{m}}/\partial l$ have some non-negligible dependence on l, that is, when the gradient is nonlinear, as it often is in practice.

As a simple example, consider optical pumping with mean photon spin $s_z=1$, which will produce a positive polarization P. For high polarizations, the rf spectrum will be dominated by the resonance $f\bar{m}=aI$ and the neighboring resonance $f\bar{m}=a,I-1$. Denote the ratio of the voltage images of these two resonances by

$$r(l')=\frac{V_{aI,j}(l')}{V_{a,I-1,j}(l')}=\frac{[I]}{2([I]-1)}\left(\frac{1+P(l')}{1-P(l')}\right). \quad (40)$$

The coefficients $M_{f\bar{m}}$ cancel out of the ratio, eliminating the difficult problem of determining all of the gains, attenuations, rf field amplitudes, etc., which enter into Eq. (36). Expression (40) is obtained by combining Eqs. (35), (39), and (16). One can readily solve Eq. (40) to find

$$P(l)=\frac{2([I]-1)r(l)-[I]}{2([I]-1)r(l)+[I]}. \quad (41)$$

In the case of ^{85}Rb, with $I=5/2$, Eq. (41) reduces to $P=(5r-3)/(5r+3)$.

C. Imaging with unresolved resonances

For semiquantitative imaging studies, it is convenient to work at such low uniform fields B_z' and such large field gradients $\partial B_z/\partial l$ that the voltage images $V_{f\bar{m},j}$ overlap and the image coordinates l' of Eq. (31) are nearly the same. All the resonances will then occur at nearly the same spatial location l and will be confined to nearly the same increment $\Delta l \ll L$ along the probe beam. The criterion for this kind of imaging is the reverse of Eq. (31)

$$\left|\frac{\partial B_z}{\partial l}\right| \gg \frac{2g_S\mu_B B_z^2}{[I]L\hbar|\omega_{\rm hf}|}. \quad (42)$$

If the uniform magnetic field B_z' is large enough for good intrinsic resolution, that is, if the criterion (11) is satisfied, the expressions (12) for the signal will remain valid and the lock-in amplifier voltage will be

$$V_j=\sum_{f\bar{m}} V_{f\bar{m},j}. \quad (43)$$

Inserting the voltages (35) into Eq. (43) and using Eq. (39) and the probe-direction coefficients (19) we find

$$V_x=MP, \quad (44)$$

$$V_y=-\frac{MP[1+\epsilon(I,P)]}{[I]}, \quad (45)$$

where the paramagnetic coefficient is

$$\epsilon(I,P)=\frac{\langle I_z\rangle}{\langle S_z\rangle}=2\langle I(I+1)-I_z^2\rangle. \quad (46)$$

The functions $\epsilon(I,P)$ depend on the nuclear spin I of the alkali-metal atom and are listed for the low values of I in Table I. Note that $\epsilon(I,0)=4I(I+1)/3$ and $\epsilon(I,1)=2I$.

Although expressions (44) and (45) were derived assuming the validity of Eq. (11), they remain valid even when Eq. (11) is violated and the resonances are only partially resolved or not resolved at all, as discussed in detail in Ref. [19]. This remarkable generality of Eq. (44) comes from a sum rule similar to the oscillator-strength sum rules of atomic or nuclear physics. The images (44) suffer substantial aberrations if the widths of the point-spread functions (33) (or their generalizations to the situation of poorly resolved resonances) are large compared to the scale lengths for variations of P within the cell.

TABLE I. Function $\epsilon(I,P)$ for low values of I.

I	$\epsilon(I,P)$
0	0
1/2	1
1	$8/(3+P^2)$
3/2	$(5+P^2)/(1+P^2)$
2	$(40+24P^2)/(5+10P^2+P^4)$
5/2	$(35+42P^2+3P^4)/(3+10P^2+3P^4)$
3	$(112+224P^2+48P^4)/(7+35P^2+21P^4+P^6)$
7/2	$(21+63P^2+27P^4+P^6)/(1+7P^2+7P^4+P^6)$

D. Polarization estimates from area ratios of gradient-free resonances

For cells with resonably uniform polarization in the illuminated volume, a convenient estimate of the polarization can be obtained from area ratios of gradient-free resonances. If Eq. (11) is valid, the lock-in voltage (6) will consist of a series of peaks $V_{f\bar{m},j}(B_z')$, which we can identify as coming from each of the resonances of Eq. (12), for example,

$$V_{a\bar{m},j}=G\frac{g_S\mu_B B_1 s_n u_{aj}}{8[I]^2\hbar}([a]^2-4\bar{m}^2)\times\int_{-L/2}^{L/2} PQ_{\bar{m}}\frac{\gamma_{a\bar{m}}}{(\omega'_{a\bar{m}}-\omega)^2+\gamma_{a\bar{m}}^2}dl. \quad (47)$$

The probe-direction coefficients u_{fj} were given by Eq. (19). The rf drive frequency ω and the resonance frequencies $\omega'_{a\bar{m}}$ are independent of position l along the probe beam, but P, $Q_{\bar{m}}$, and $\gamma_{a\bar{m}}$ may all depend on l. We may define peak areas by

$$A_{f\bar{m},j}=\int_{-\infty}^{\infty} V_{f\bar{m},j}dB_z' =\frac{\pi G B_1 s_n u_{fj}}{8[I]}([a]^2-4\bar{m}^2)\int_{-L/2}^{L/2} PQ_{\bar{m}}dl. \quad (48)$$

We have used the approximation, typically accurate to better than 1%, $|\partial\omega_{f\bar{m}}/\partial B_z|=g_S\mu_B(\hbar[I])^{-1}$ in evaluating the integral over dB_z'. We see that the areas (48) are averages along the probe beam of the products $PQ_{\bar{m}}$, which from Eq. (16) are complicated rational functions of P. However, if the overall polarization does not vary much along the probe beam, for example, because a uniform pumping beam is used, we can approximate the integral by the product of the probe length L and a function of an effective polarization $\bar{P}$,

$$\int_{-L/2}^{L/2} P Q_{\bar{m}} dl \approx L \overline{P} Q_{\bar{m}}(\overline{P}). \tag{49}$$

Then we can take area ratios, in analogy to Eq. (40), to find

$$\overline{r} = \frac{A_{aI,j}}{A_{a,I-1,j}} = \frac{[I]}{2([I]-1)} \left(\frac{1+\overline{P}}{1-\overline{P}} \right). \tag{50}$$

Solving Eq. (50) with the aid of Eq. (16) we find

$$\overline{P} = \frac{2([I]-1)\overline{r} - [I]}{2([I]-1)\overline{r} + [I]}, \tag{51}$$

in complete analogy to Eq. (41).

Thus one can use Eq. (51) to make a convenient and simple estimate of the polarization from the area ratio $\overline{r}$ of gradient-free resonances. No gradient coils are needed. The rf field amplitude, various gains, optical losses, and other factors that are difficult to measure cancel out of the area ratio. For the effective polarization $\overline{P}$ to be easily interpreted, it is necessary that $P(l)$ (or, equivalently, the intensity of the pumping light) be reasonably uniform over the length L of the probe beam and that $P(l)$ be negligibly small elsewhere. If $P(l)$ varies substantially along the probe beam, the spatial variation may be determined by the gradient-imaging methods outlined above.

E. Effects of spatial diffusion

The discussion so far has ignored the spatial diffusion of the precessing atoms that produce the images. In [19] it is shown that the simple Lorentzian point-spread function (26) is appropriate for field gradients $\partial\omega_0/\partial l$ much less than the crossover gradient

$$\left(\frac{\partial \omega_0}{\partial l} \right)_c = \sqrt{\frac{\gamma_0^3}{D}}. \tag{52}$$

In the experiments discussed in this paper, the diffusion coefficients are $D \sim 0.04$ cm^2 s^{-1} for both the He and Xe cells discussed below. Representative damping rates, dominated by the rapid optical-pumping rate R in Eq. (18), would be $\gamma_0 \sim 10^5$ s^{-1}. Then the crossover Larmor-frequency gradient would be $(\partial\omega_0/\partial l)_c = 1.58 \times 10^8$ s^{-1} cm^{-1}. In view of Eq. (9), for ^{85}Rb with $I = 5/2$, the crossover magnetic-field gradient would be $\nabla B_z = 54$ G cm^{-1}, which is much larger than any gradients actually used. A discussion of the appropriate generalization of the point-spread function (26) or (33) for very large gradients $\partial\omega_0/\partial l \gg (\partial\omega_0/\partial l)_c$ can be found in [19].

III. EXPERIMENTAL APPARATUS

The experimental apparatus is presented in Fig. 3. We used two different high-pressure Rb optical-pumping cells: a ''Xe'' cell, a glass cylinder with an inner diameter of 2.4 cm and a length of 8 cm filled with 7.8 atm at 20 °C of 1.34% Xe (natural isotopic composition), about 0.7% N_2, and ^{4}He and a ''He'' cell, a glass sphere of 2.0 cm inner diameter

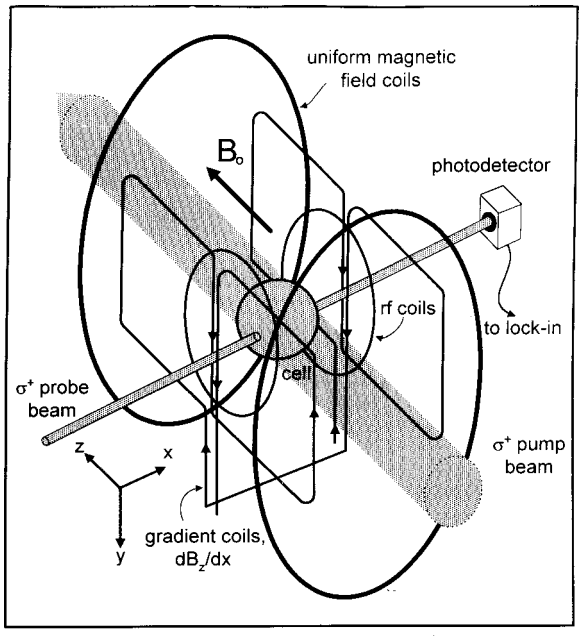

FIG. 3. Experimental apparatus. The total magnetic field B is the resultant of a uniform field B_z' and a linear gradient field $[x(\partial B_z/\partial x)]$, both along the z axis. The lock-in signal arises solely from the Rb spins in resonance. As B_z' is swept linearly in time, the volume element in resonance is swept along the x axis.

filled to 13.5 atm (at 20 °C) mixture of 70 torr N_2 and ^{3}He. The glass cells were placed in a hot-air oven to maintain the desired Rb number densities for optical pumping. The equilibrium saturated vapor pressure was attained with a few milligrams of natural Rb metal. The operational temperature range was from 60 °C to 180 °C. We used two different lasers for Rb optical pumping. One laser was an Opto Power Corp. ''150 W'' cw water-cooled stack of 10 $Al_xGa_{1-x}As/GaAs$ laser diode arrays with an overall spectral width of approximately 4 nm FWHM. Under our operating conditions, the maximum laser power was 80 W at the 795-nm Rb D_1 line. The 90% linearly polarized laser beam was collimated and directed into the cell by two antireflection coated cylindrical lenses. Due to the difficulty in properly collimating and directing the beam and due to the reflections from the uncoated oven and cell windows, approximately 30% of the laser power got into the cell. The second laser was an Opto Power Corp. B015 fiber-optic coupled diode laser, emitting 9 W of unpolarized laser beam at 795 nm, with approximately 2.5 nm spectral linewidth, FWHM. This beam was collimated by two uncoated aspherical lenses. Although the fiber-optic coupled laser diode produced a more collimated beam, we estimate that only approximately 40% of the initial laser power got into the cell, due to the initially unpolarized laser beam and to the uncoated optics and windows. The collimated laser beams have been linearly polarized by a beam splitter cube and circularly polarized by a $\lambda/4$ wave plate. Due to the broad spectral emission of the diode lasers, only a fraction of the laser power reaching the cell actually contributes to optical pumping. The beam crosses the cell along a uniform static magnetic field B_z', which defines the z axis of the coordinate

system. The magnetic field of 4 G (low-field regime) and up to 31–38 G (high-field regime) is produced by a pair of 1.5-m-diam Helmholtz coils. A circularly polarized Ti:sapphire laser probe beam propagating perpendicularly to the pump beam defines the x axis of the coordinate system. The Ti:sapphire laser was operated at 795 nm, or detuned by a few tens of nanometers in order to maintain the absorption by the vapor in the order of 10%. The intensity of this beam was varied from 1 to 30 mW for the different measurements. The transmitted intensity of the probe beam was monitored by a fast photodiode operated in the photoconductive mode. A modulating rf field of 0.1 to 10 mG amplitude, along the x axis, was produced by a pair of 12-cm-diam Helmholtz coils concentric with the probe beam, mounted on either side of the oven. The coils have been driven by a 40-db rf amplifier coupled to a digital function generator. Radio-frequency current was applied to the coils and tuned to the Bohr condition for transitions between the Zeeman sublevels $|f,m\rangle$ and $|f,m-1\rangle$. The rf field generated coherence between the sublevels and an associated transverse magnetization rotating in synchrony with the rf [16]. The precessing ^{85}Rb spin polarization modulated the transmission of the circularly polarized probe beam at the rf frequency as described in Sec. II. The transmission was monitored by a lock-in amplifier with the rf frequency as reference and recorded by a digital oscilloscope. When the magnitude of the magnetic field B_z' was swept through the Rb Zeeman resonances, the transmitted probe beam exhibited resonances corresponding to the ^{85}Rb polarization along the probe-beam path. The areas and the linewidths of different transitions have been determined from these measurements by calibrating the sweep rate.

For imaging the ^{85}Rb polarization in high-pressure optical-pumping cells a constant gradient $(\partial B_z/\partial x)$ was added to the static magnetic field B_z'. The gradient was generated by two squared figure-eight-shape coils mounted on both sides of the oven (Fig. 3). The two central, linear, parallel conductors of this mount, with current flowing in the same direction, generate a 67-mG/(cm A) gradient in the cell. For high-resolution imaging we used gradients as high as 1 G/cm. Under these conditions, the frequency of the rotating transverse magnetization depends on position along the probe axis. Sweeping the magnitude of the B_z' field causes the resonant surface to move along the probe beam from one side of the cell to the other. Thus the modulation amplitude of the transmitted probe beam depends on the polarization along the probe beam and a submillimeter spatial resolution in imaging the alkali-metal polarization is achievable. With a narrow probe beam one can scan over the y-z axes to obtain a three-dimensional polarization image.

The atomic linewidth of ^{85}Rb in the high-pressure cells (0.4 nm FWHM in the 13.5-atm cell and 0.29 nm in the 7.8-atm cell), as well as the total gas pressure and the ^{85}Rb number density, have been measured by scanning the frequency of a linearly polarized Ti:sapphire probe beam over the resonance at 794.8 nm and monitoring the transmission [23]. The 1.34% Xe fraction in the gas mixture used to fill the cell was measured by freezing the Xe in the mixture in a test cell with liquid N_2, evacuating the unfrozen gas and then warming the cell to room temperature and measuring the pressure.

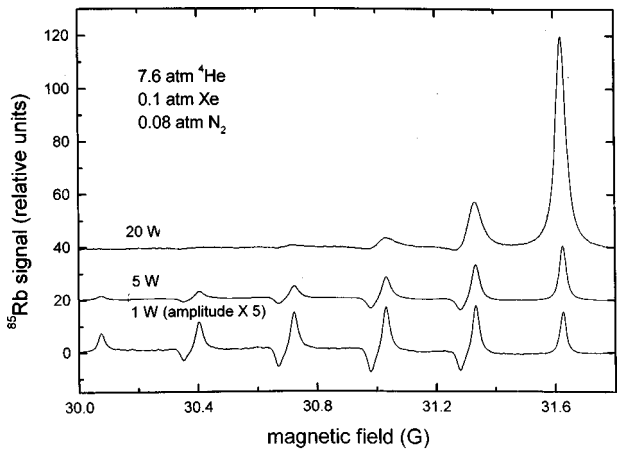

FIG. 4. ^{85}Rb signal with high magnetic field ($B_z' \approx 31$ G), in the absence of an imaging gradient, for 1, 5, and 20 W of optical pumping power from the Opto Power stack of diode arrays. All ten Zeeman transitions of both the $f=3$ and $f=2$ hyperfine multiplets are well resolved and the signal amplitudes of the resonance peaks are in excellent agreement with the spin-temperature prediction of Eq. (12).

IV. EXPERIMENTAL RESULTS

A. Evaluation of the absolute Rb polarization

A spin-temperature distribution of the populations in the Rb spin sublevels $|f,m\rangle$ was found in our high-pressure cells [16]. Figure 4 displays three representative signals for a uniformly pumped Xe cell, with laser powers of 1, 5, and 20 W. Similar traces have been measured in the He cell. The ^{85}Rb transmission signals measured with high magnetic field B_z' ≈ 31 G and without an imaging magnetic field gradient, show all ten Zeeman transitions in the $f=3$ (six positive peaks) and $f=2$ (four negative peaks) hyperfine multiplets as described by Eq. (35), for $j=x$. The signal amplitudes of the resonance peaks closely obey the spin-temperature limit $\rho=\exp(\beta F_z)/Z$ regardless of the relatively small rate of Rb-Rb spin-exchange collisions compared to the high rate of spin destruction by electron-randomizing collisions with buffer-gas atoms at high pressure. We calculated the areas $A_{5/2}$ and $A_{3/2}$ of the peaks related to the Zeeman transitions $f=3$, $\bar{m}=5/2$ and $f=3$, $\bar{m}=3/2$ by numerical integration of the signal or through a best fit of Eq. (35) to the experimental traces and calculated the absolute polarization using Eq. (51). In calculating the signal areas, one should eliminate the part of the signal related to the transition $f=2$, $\bar{m}=3/2$ interfering with the $f=3$, $\bar{m}=3/2$ transition by the numerical best fit or experimentally by applying a rotating rf field rather than the linear rf field of our case. Figure 5 presents the effective-absolute Rb polarization as a function of the pump-laser power calculated by Eq. (51). Figure 5(a) presents the effective-absolute polarization in the Xe cell and Fig. 5(b) the effective-absolute polarization in the He cell. The dots are experimental values and the solid lines represent best-fit calculated values based on Eq. (18) with the spin destruction rates $T_{\mathrm{SD}}^{-1}=30\,000\ \mathrm{s}^{-1}$ and $\alpha=3200\ \mathrm{J}^{-1}$ for the Xe cell ($T=100\,^{\circ}\mathrm{C}$) and $T_{\mathrm{SD}}^{-1}=510\ \mathrm{s}^{-1}$ and $\alpha=7000\ \mathrm{J}^{-1}$ for the He cell. The spin destruction rates T_{SD}^{-1}

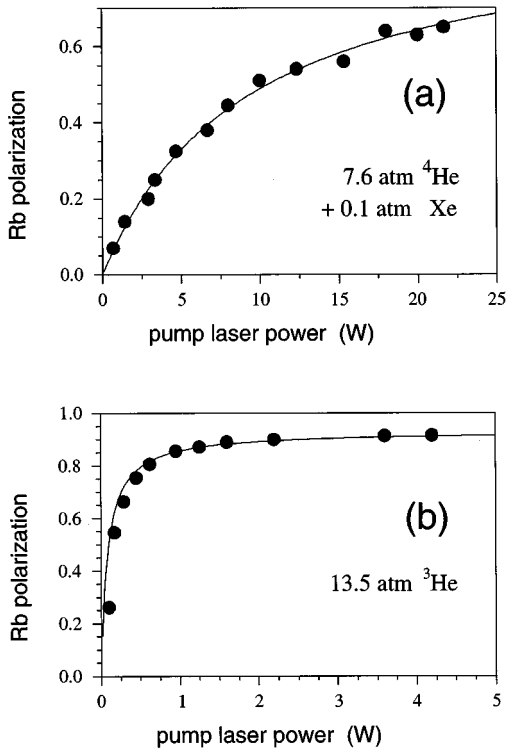

FIG. 5. Absolute Rb polarization P as a function of laser power I_l for (a) the Xe cell at $T=100\,^{\circ}\mathrm{C}$ and (b) the ^{3}He cell at $T=130\,^{\circ}\mathrm{C}$. The measured values (circles) fit well to the function (18) with $s_z=0.94$ and $R=\alpha I_l$. The parameters are $\alpha=7000\ \mathrm{J}^{-1}$ and $T_{\mathrm{SD}}^{-1}=30\,000\ \mathrm{s}^{-1}$ for the Xe cell and $\alpha=3200\ \mathrm{J}^{-1}$ and $T_{\mathrm{SD}}^{-1}=510\ \mathrm{s}^{-1}$ for the ^{3}He cell.

have been determined by measuring the electron spin relaxation in the dark [24]. The mean photon spin s_z, which in our case is $s_z=0.94$, reflects the imperfect circular polarization of the pump lasers.

B. Rb magnetic resonance linewidth

The knowledge of the magnetic resonance linewidth of the different Rb Zeeman transitions is important in order to determine the maximum possible spatial resolution of a polarization image [see Eq. (34)]. We investigate the Rb linewidth as a function of the pump-laser intensity. A more complete analysis of Rb linewidth measurements, including light-narrowing phenomena and calculations, will be presented elsewhere [19,25].

Figure 6 shows the results of the measured ^{85}Rb linewidth (FWHM) of the Zeeman transition $f=3$, $\bar{m}=5/2$ as a function of the pump-laser power for the two cells used in this experimental work, the Xe cell and the He cell, at 100 °C, measured with a magnetic field of $B_z'=31$ G. The circles are experimental values and the solid lines are derived from the model represented by Eq. (17) [19]. In these measurements, the Xe cell was homogeneously pumped by the stack of diode arrays. We used different concentrations of $CuSO_4$ water solutions to reduce the laser power pumping the Xe cell. From 0.6 W up to 3 W the linewidth is aproximately 7 kHz and then increases to nearly 13 kHz at 20 W. Therefore, the expected spatial resolution of a polarization image at full

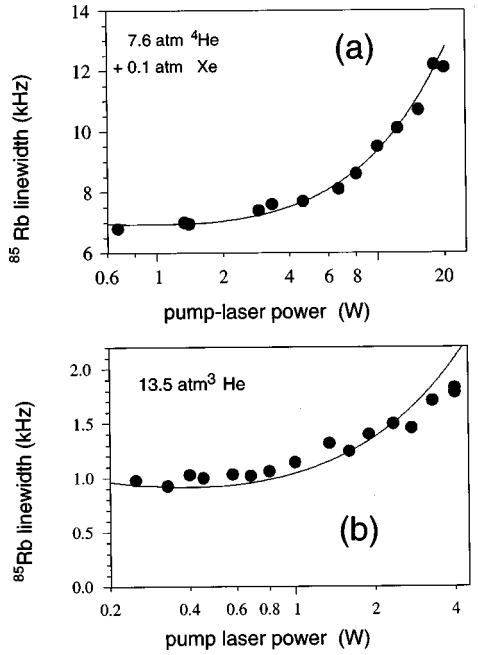

FIG. 6. ^{85}Rb linewidth for the $f=3$, $\bar{m}=5/2$ transition versus pump-laser power for (a) 7.6 atm ^{4}He, 0.09 atm N_2, and 0.1 atm Xe gas pressure (Xe cell) and (b) 13.5 atm ^{3}He and 0.09 atm N_2 gas pressure and no xenon (^{3}He cell).

pumping power in low magnetic field, with $\gamma_{3,5/2}/\pi=13$ kHz and a gradient of 1 G/cm, is 0.3 mm [see Eq. (34)]. For the high magnetic field of $\approx$38 G used in our high-field images, the maximum spatial resolution calculated from Eqs. (32) and (34) is 1.3 mm.

The He cell was pumped by a laser beam from the fiber-optics coupled diode-laser array, fully illuminating the cell. The pumping power was reduced by neutral-density filters. Great care was taken in order to minimize possible broadening mechanisms, such as the pumping by the detection-laser beam and residual magnetic field gradients. The smallest measured linewidth ($\approx$1 kHz) is 7 times smaller than in the Xe cell, although the total pressure of the He cell (13.5 atm) is much higher than in the Xe cell. The linewidth increases with the pump power up to 1.7 kHz. The 7 times narrower Rb linewidth in the ^{3}He cell compared to the Xe cell has the consequence that the maximum resolution in an Rb-imaging experiment is expected to be much higher for He cells, as will be shown later. The spatial resolution at full pumping power, in low magnetic field and in a gradient of 1 G/cm, is below 100 μm [Eq. (34)]. For $B_z'=38$ G, the spatial resolution calculated from Eq. (34) is 0.17 mm.

C. Rb-polarization imaging

1. Low-field imaging of Rb polarization

By applying gradient fields, it is possible to evaluate the influence of nonuniform illumination on the Rb polarization present in the optical-pumping cell. Figure 7 shows two examples for low-field images of ''homogeneously'' illuminated cells, one for the Xe cell [Fig. 7(a)] and another for the He cell [Fig. 7(b)]. To demonstrate the high spatial resolution achievable in the He cell, we blocked the pump beam

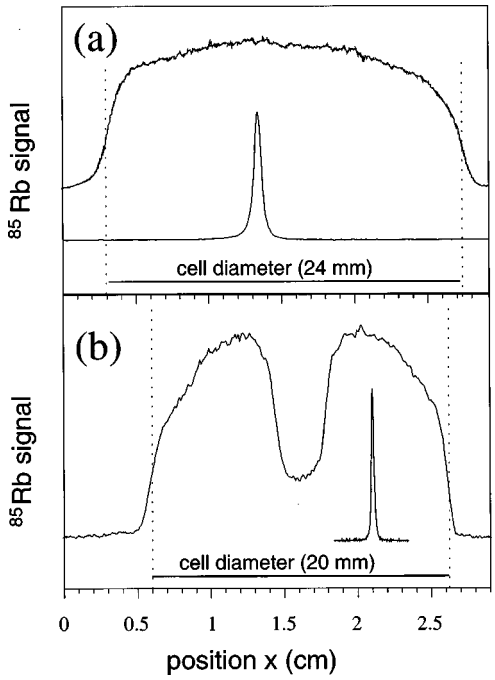

FIG. 7. (a) Low-field Rb image for the case of a homogeneously illuminated Xe cell with a diameter of 24 mm. The point-spread function obtained from a low-field magnetic sweep measurement (no gradient present) indicates a spatial resolution of about 0.7 mm. (b) Low-field Rb image for the ^{3}He cell with a diameter of 20 mm. The ''hole'' in the image reflects a 4-mm stripe placed in front of the cell blocking a part of the pump-laser beam. Compared to (a), the point spread function is much narrower and results in a resolution of 0.11 mm.

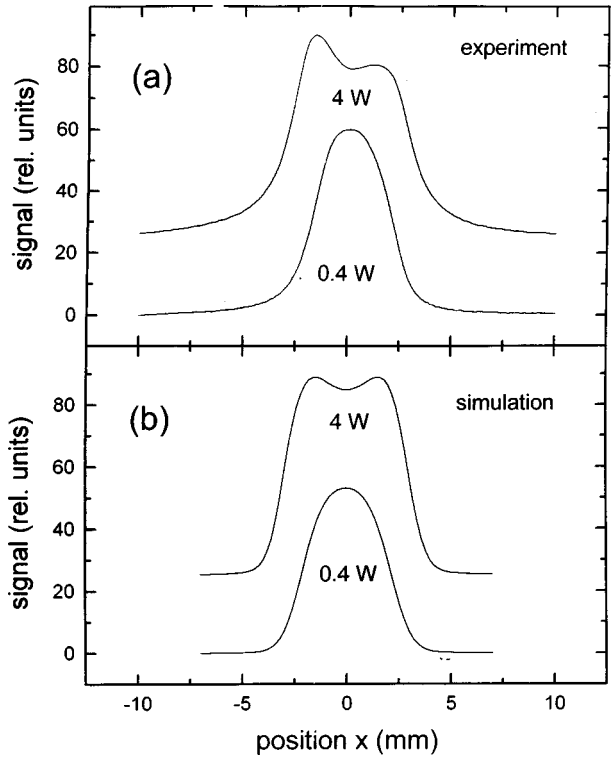

FIG. 8. (a) Low-field Rb image (4 G) of a Xe cell pumped by a fiber-optic coupled diode laser beam with a bell-shape beam profile and 3 mm diameter FWHM. The upper trace is for a pump-laser power of $I_l = 4$ W, the lower trace for $I_l = 0.4$ W. The applied magnetic field gradient was 0.4 G/cm for the two cases. (b) Numerical simulation for the two cases depicted in (a) with an assumed Gaussian pump-laser beam with a FWHM of 2.7 mm, a maximum optical pumping rate of 10^6 s^{-1} for the 4-W power (10^5 s^{-1} for 0.4 W), $T_{SD}^{-1} = 30\,000$ s^{-1}, $T = 100$ °C, $\gamma_{3,5/2} \approx 7/12 T_{SD} + R/6$, and a magnetic field gradient of 0.4 G/cm.

along a 4-mm-thick stripe in front of the cell. As shown in Sec. II, these images are a direct measurement of the relative polarization along the x axis, $V(x) \propto P(x)$. For both images the rf frequency was kept constant at 2 MHz, the magnetic field gradient was 0.54 G/cm for the Xe cell (0.67 G/cm for the He cell), and the static field B_z' was swept in 90 s from 3.43 G to 5.17 G. Below the low-field images we show the Rb signal obtained from the magnetic field scan without an applied field gradient. This measured peak, with an almost Lorentzian shape, can be transformed into the point-spread function [Eq. (26)] by knowing the sweeping range of the static magnetic field and the field gradient used for the image. The linewidth of the point-spread function (FWHM) allows a direct, experimental evaluation of the achievable spatial resolution. In our case the spatial resolution is 0.7 mm for the Xe cell and 0.11 mm in the He cell.

Figure 8(a) shows imaging signals in low field (4 G) at $T = 100$ °C, of the polarization produced by an $\sim$3-mm (FWHM) bell-shaped beam from the fiber-optic coupled diode laser. The upper (lower) trace was measured with 4 W (0.4 W) of pump-laser power incident on the cell. The images have been obtained by scanning the magnetic field B_z' at a fixed rf frequency of 2 MHz. The Ti:sapphire probe beam had a diameter of ≈ 2 mm (30 mW power) and the applied magnetic field gradient was $\partial B_z / \partial x = 0.4$ G/cm. The lower trace in Fig. 8(a) reflects the beam shape, but in the upper trace (4 W pump-laser power) a ''hole'' occurs at $x = 0$ cm. In this case, the Rb line is broadened considerably due to optical pumping and the Rb polarization does not increase anymore as it reaches the saturation value of about 94%. The width of the point spread function is large compared to the scale lengths for variations of P and therefore the signal is no longer proportional to the polarization. The asymmetry of this trace reflects a slightly asymmetric pump-laser profile. Through extensive simulations of the imaging signals under various illumination conditions, we found that the imaging signal described by Eq. (43) can be well approximated by using only the term related to the Zeeman transition $f = 3$, $\overline{m} = 5/2$ of Eq. (12) in calculating $\overline{\langle S_n \rangle}$, with $Q_{5/2} \equiv 1$. Figure 8(b) shows a simulation of the imaging signals calculated by Eq. (43) with this approximation, using a Gaussian pumping beam with a FWHM of 2.7 mm, and all other parameters similar to the real experiment: $T = 100$ °C, optical-pumping rate $R = 2.5 \times 10^5$ s^{-1} for 1 W pumping power, $T_{SD}^{-1} = 30\,000$ s^{-1} (Xe cell), and $\partial B_z / \partial x = 0.4$ G/cm.

2. High-field imaging of Rb polarization

The low-field images show the Rb-polarization distribution in the optical-pumping cell with high resolution and a good signal-to-noise ratio. However, the spatial resolution is limited by the maximum applicable magnetic field gradient

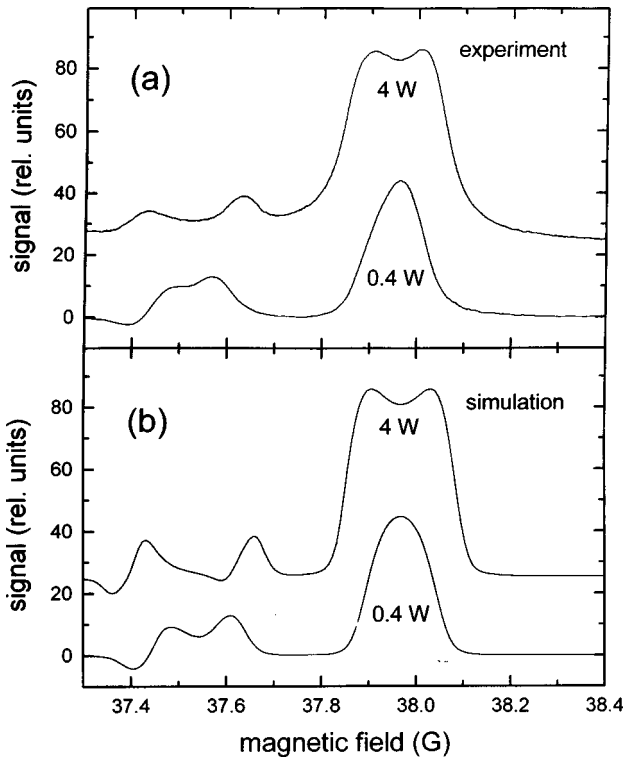

FIG. 9. (a) High-field Rb image ($\sim$38 G) of the Xe cell pumped under similar conditions as in the low-field experiment described in Fig. 8. The two high-field traces in (a) show two resonances of ^{85}Rb, with $f=3$ and $\bar{m}=5/2$ and 3/2 . (b) Numerical simulation for the two cases depicted in (a) with the same numerical parameters as in Fig. 8(b) and $\gamma_{3,3/2}\approx 25/36T_{SD}+4R/9$.

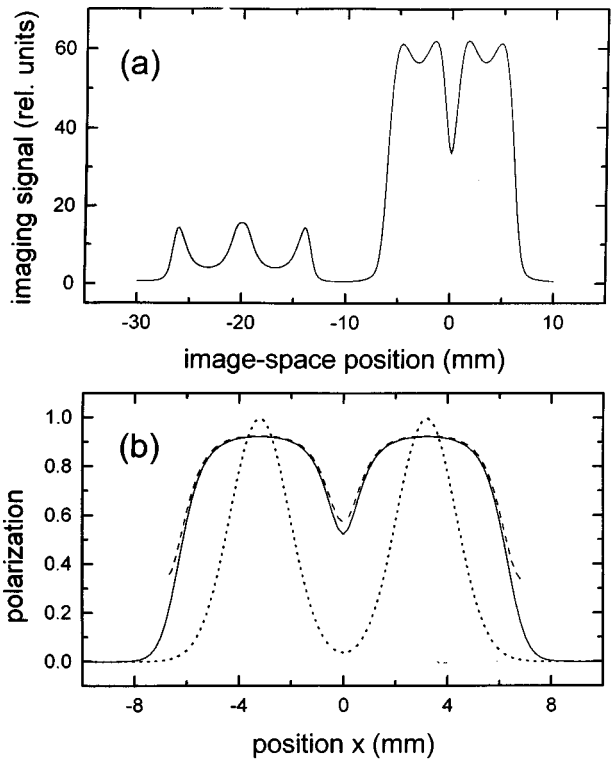

FIG. 11. High-field ($\sim$38 G) numerical simulation for an extreme optical pumping case in a Xe cell: two Gaussian pumping beams of 10^6-s^{-1} maximum optical pumping rate and a FWHM of 2.7 mm, 3.2 mm apart from each other, and 0.4 G/cm. (a) $f=3$ with $\bar{m}=3/2$ and 5/2 transitions in the ''imaging voltage'' signal. (b) Polarization calculated by Eq. (41) from the ratio of the voltages $V_{3,5/2,x}/V_{3,3/2,x}$ (dashed line), along with the absolute polarization (solid line) and the optical-pumping rate (dotted line).

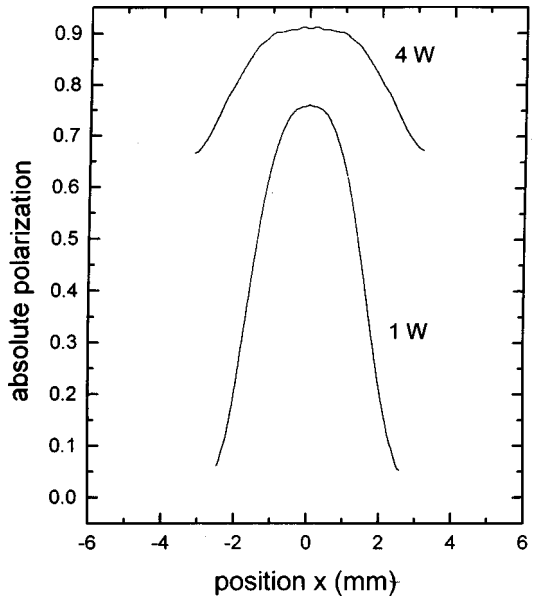

FIG. 10. Image of the absolute Rb polarization along the probe beam. The polarization was calculated from the ratio of the voltages $V_{3,5/2,x}/V_{3,3/2,x}$ of the $f=3$ and $\bar{m}=5/2$ and 3/2 transitions as measured in high magnetic field (38 G) and presented in Fig. 9(a), by Eq. (41). The upper trace is for $I_l=4$ W, the lower for $I_l=0.4$ W.

due to the ''low-field'' condition of Eq. (31). In order to determine the absolute Rb-polarization distribution from the low-field images, it is necessary to measure the absolute transmission too. These difficulties can be elegantly avoided by measuring the Rb polarization in a high field. Figure 9(a) displays the experimental results in a high field (38 G) under experimental conditions similar to those in Fig. 8(a): two pump-laser powers 4 W and 0.4 W, a 3-mm (FWHM) bell-shaped profiled pump beam, $T=100$ °C, and $\partial B_z/\partial x=0.4$ G/cm. The high-field images have been obtained by scanning the magnetic field B_z' at the fixed rf frequency of 17.2 MHz. Only three transitions $f=3$, $\bar{m}=5/2$, $f=3$, $\bar{m}=3/2$, and $f=3$, $\bar{m}=3/2$ are displayed. The $f=3$, $\bar{m}=5/2$ transition in the 4-W trace shows a hole formed at $B_z'=38$ G, which is similar to the hole shown in the low-field image in Fig. 8(a). This hole appears as a result of the large width of the point-spead function. The $f=3$, $\bar{m}=3/2$ transition has a deep hole around 37.53 G even at low pump power. Figure 9(b) is a numerical simulation for high-field images (38 G), with the same parameters as in Fig. 8(b). These simulations show the essential shape and features of the experimental traces of Fig. 9(a), including the hole in the $f=3$, $\bar{m}=5/2$ transition.

From the ratio of the signal voltages of the $f=3$, $\bar{m}=5/2$ and $f=3$, $\bar{m}=3/2$ transitions in Fig. 9(a), at corresponding magnetic-field positions, the absolute Rb polarization can be evaluated by Eq. (41). The result is shown in Fig.

10 for the two cases depicted in Fig. 9(a). We used only the right part from the center of both transitions (at 37.53 and 37.99 G) for this calculation, as the $f=2$, $\bar{m}=3/2$ transition of the $f=2$ hyperfine level interferes with the left part of the $f=3$, $\bar{m}=3/2$ transition. For display only, the result of this procedure was then mirrored at $x=0$ mm, assuming that the pump-laser intensity profile is symmetric with respect to $x=0$. Although we mentioned in Sec. II that Eq. (41) is valid for the case that the width of the point-spread function is small compared to the scale lengths for variations of P and therefore the signal is no longer proportional to the polarization (which is not the case in the 4-W illumination), we found through simulations that Eq. (41) is a good approximation in most practical optical-pumping applications (with optical-pumping rates from zero to 10^6 s^{-1}). The two graphs depicted in Fig. 10 show again a bell shape for the absolute Rb polarization and the hole appearing in Figs. 8(a) and 9(a) disappears. Note that the absolute polarization around $x=0$ saturates to a value of 94%. This value is in good agreement with the saturation value $s_z=0.94$ obtained in Fig. 5(a).

Figure 11 shows a high-field simulation of an extreme optical-pumping case: a Xe cell pumped by two parallel Gaussian beams each with a FWHM of 2.7 mm, 3.2 mm apart, each with a maximum pumping rate of 10^6 s^{-1}. Figure 11(a) displays the ''voltage-imaging'' signal of the transitions $f=3$, $\bar{m}=5/2$ and $f=3$, $\bar{m}=3/2$. Figure 11(b) shows the calculated absolute polarization using the voltage ratios as given by Eq. (41), along with the absolute polarization calculated by Eq. (18) and the optical-pumping rate produced by the two Gaussian beams. The similarity between the absolute polarization calculated by the two equations emphasizes the applicability of Eq. (41).

V. CONCLUSIONS AND OUTLOOK

We have demonstrated that it is possible to image the absolute Rb polarization in high-pressure optical-pumping cells with resolutions down to 100 μm. Our determination of the absolute Rb polarization makes use of the helpful fact that optical pumping under the high-pressure conditions considered in this work always establishes a spin-temperature distribution among the Rb hyperfine levels. This is true even without the assumption of rapid Rb-Rb spin-exchange processes and narrow-band pump lasers. We presented measurements of the magnetic-resonance linewidths, especially important to predict the maximum possible spatial resolution for gas-phase polarization images. Finally, we presented experimental results of polarization images for different buffer-gas compositions and for various conditions of pump-laser illuminations along with results from imaging simulations.

It is likely that the technique we used for imaging the absolute Rb polarization is not restricted to the gas phase, but can also be applied to atoms that are embedded in optically transparent solids or liquids. Furthermore, it should be possible to image the polarization of optically pumped atoms interacting with a surface, giving information about the Rb-polarization distribution and the Rb-relaxation mechanisms on the surface.

ACKNOWLEDGMENTS

This work was supported by the AFOSR and the Defense Advanced Research Project Agency, with assistance from the Princeton cyclotron group, funded by the NSF.

[1] M. S. Albert, G. D. Cates, B. Driehuys, W. Happer, B. Saam, C. S. Springer, and A. Wishnia, Nature (London) **370**, 188 (1994).

[2] H. Middleton, R. D. Black, B. Saam, G. D. Cates, G. P. Cofer, R. Guenther, W. Happer, L. W. Hedlund, G. A. Johnson, K. Juvan, and J. Swartz, Magn. Reson. Med. **33**, 271 (1995).

[3] R. D. Black, H. Middleton, L. W. Hedlund, M. D. Shattuck, G. A. Johnson, J. Swartz, B. Driehuys, G. D. Cates, G. P. Cofer, and W. Happer, Radiology **199**, 867 (1996).

[4] M. Ebert, T. Broßman, W. Heil, E. Otten, R. Surkau, M. Leduc, P. Bachert, N. V. Knopp, R. Schad, and M. Thelen, Lancet **347**, 1297 (1996).

[5] M. E. Wagshul, T. M. Button, H. F. Li, Z. Liang, K. Zhong, and A. Wishnia, Magn. Reson. Med. **36**, 183 (1996).

[6] J. R. MacFall, H. C. Charles, R. D. Black, H. Middleton, J. Swartz, B. Saam, B. Driehuys, C. Erickson, W. Happer, G. D. Cates, G. A. Johnson, and C. E. Ravin, Radiology **200**, 553 (1996).

[7] G. Navon, Y.-Q. Song, T. R$\tilde{o}\tilde{o}$m, S. Appelt, R. E. Taylor, and A. Pines, Science **271**, 1848 (1996).

[8] T. R$\tilde{o}\tilde{o}$m, S. Appelt, R. Seydoux, E. L. Hahn, and A. Pines, Phys. Rev. B **55**, 11 604 (1997).

[9] B. Driehuys, G. D. Cates, and W. Happer, Phys. Lett. A **184**, 88 (1993); B. Driehuys, G. D. Cates, and W. Happer, Phys. Rev. Lett. **74**, 4943 (1995).

[10] H. W. Long *et al.*, J. Am. Chem. Soc. **115**, 8491 (1993).

[11] B. Driehuys, G. D. Cates, E. Miron, K. Sauer, D. K. Walter, and W. Happer, Appl. Phys. Lett. **69**, 1668 (1996).

[12] T. E. Chupp *et al.*, Phys. Rev. Lett. **72**, 2363 (1994); R. E. Stoner *et al.*, *ibid.* **77**, 3971 (1996).

[13] S. Appelt, G. Waeckerle, and M. Mehring, Phys. Lett. A **204**, 210 (1995); Phys. Rev. Lett. **72**, 3921 (1994).

[14] P. L. Anthony *et al.*, Phys. Rev. Lett. **71**, 959 (1993).

[15] J. Skalla, G. Waeckerle, M. Mehring, and A. Pines, Phys. Lett. A **226**, 69 (1997).

[16] A. R. Young, S. Appelt, A. Ben-Amar Baranga, C. Erickson, and W. Happer, Appl. Phys. Lett. **70**, 3081 (1997).

[17] E. L. Hahn, Phys. Rev. **80**, 580 (1950).

[18] H. Kopfermann, *Nuclear Moments* (Academic, New York, 1958).

[19] S. Appelt, A. Ben-Amar Baranga, C. J. Erickson, M. V. Romalis, A. R. Young, and W. Happer, Phys. Rev. A **58**, 1412 (1998).

[20] L. Wilmer Anderson, Francis M. Pipkin, and James C. Baird, Phys. Rev. **116**, 87 (1959).

[21] S. Kadlecek, L. W. Anderson, and T. G. Walker, Phys. Rev. Lett. **80**, 5512 (1998).

[22] J. D. Gaskill, *Linear Systems, Fourier Transforms, and Optics* (Wiley, New York, 1978).

[23] M. V. Romalis, E. Miron, and G. D. Gates, Phys. Rev. A **56**, 4569 (1997).

[24] A. Ben-Amar Baranga, S. Appelt, M. V. Romalis, C. J. Erickson, A. R. Young, G. D. Cates, and W. Happer, Phys. Rev. Lett. **80**, 2801 (1998).

[25] S. Appelt, A. Ben-Amar Baranga, A. R. Young, and W. Happer (unpublished).